Available online at www.sciencedirect.com
SCIENCE DIRECT®
Journal of Sound and Vibration 292 (2006) 854–868
JOURNAL OF SOUND AND VIBRATION
www.elsevier.com/locate/jsvi

Active smart material control system for buffet alleviation

Essam F. Sheta[a,*], Robert W. Moses[b], Lawrence J. Huttsell[c]

[a]CFD Research Corporation, 215 Wynn Drive, Huntsville, AL 35805, USA
[b]NASA Langley Research Center, Hampton, VA, USA
[c]Air Force Research Laboratory, WPAFB, Dayton, OH, USA

Received 26 July 2004; received in revised form 1 August 2005; accepted 6 September 2005
Available online 2 November 2005

Abstract

Vertical tail buffeting is a serious multidisciplinary problem that limits the performance and maneuverability of twin-tail fighter aircraft. The buffet problem occurs at high angles of attack when the vortical flow breaks down ahead of the vertical tails resulting in unsteady and unbalanced loads on the tails leading to their premature fatigue failure. An active smart material control system, using distributed piezoelectric (PZT) actuators, is developed for buffet alleviation and is presented. The surfaces of the vertical tail are equipped with PZT actuators to control the buffet responses in the first bending and torsion modes. The electrodynamics of the PZT actuators are modeled using a finite-element model. A single-input/single-output controller is designed to drive the active PZT actuators. High-fidelity analysis modules for the fluid dynamics, structural dynamics, electrodynamics of the PZT actuators, control law, fluid–structure interfacing, and grid motion are integrated into a multidisciplinary computing environment that controls the temporal synchronization of the analysis modules. The results of this study indicate that the actively controlled PZT actuators are an effective tool for buffet alleviation over wide range of angels of attack. Peak values of power spectral density of tail-tip acceleration are reduced by as much as 22% in the first bending mode and by as much as 82% in the first torsion mode. The root mean square values of tail-tip acceleration are reduced by as much as 12%.
© 2005 Elsevier Ltd. All rights reserved.

1. Introduction

The ability of twin-tail fighter aircraft to fly and maneuver at very high angles of attack depends mainly on the interaction between the strong vortical flow and the vertical tails to maintain stability of the aircraft. However, at high angles of attack, the vortices that emanate from the leading-edge extension (LEX) of the wing break down upstream of the vertical tails. The breakdown vortical flow impinges upon the vertical tails resulting in severe dynamic buffet loads [1–5]. The breakdown flow contains significant amount of energy over a frequency bandwidth that often coincide with the predominant structural modes of the vertical tails. The buffet loads, imposed upon the vertical tails, result in a premature failure of the vertical tails and increased the inspection and maintenance cost of fighter aircraft.

*Corresponding author. Tel.: +256 726 4869; fax: +256 726 4806.
E-mail address: efs@cfdrc.com (E.F. Sheta).

0022-460X/$ - see front matter © 2005 Elsevier Ltd. All rights reserved.
doi:10.1016/j.jsv.2005.09.002

There are essentially two major techniques to control the tail buffet problem: flow control or structural control. The flow control methods aim into modifying the vortical flowfield around the vertical tails to reduce the buffet loads. Passive flow control [6–9] and active flow control [10,11] methods have been proposed, but only the passive methods received the most attention. For example, as a near term solution to the buffet problem of the F/A-18 aircraft, passive stream-wise LEX fence devices were used. The fences were fitted over the upper surface of the wing LEX to reconstruct the vortical flow over the aircraft [6]. The fences, although developed through trial and error wind-tunnel experiments, reduced the buffet loads experienced by the vertical tails. In flight tests by Lee et al. [7], the LEX fences reduced the acceleration peaks, at a point close to the tip of the vertical tail, from 450 to 200 g. However, a loss of 3% of maximum lift was monitored. The fences were also less effective at high angles of attack. Other passive flow control methods, such as dorsal fin extension or up-deflected LEX, have been proposed by Rao et al. [8]. Although these methods provided some buffet relief, an aerodynamic penalty was imposed on the aircraft. In addition, these methods were not effective at all flight conditions.

Active control of the tail structure can be achieved using either active control of the tail rudder [12,13] or using piezoelectric (PZT) actuators [14,15]. In the active rudder method, the rudder is deflected in response to a feed back signal from the motion of the tail tip. Moses [13] applied the active rudder concept to 1/6-scale model of the F/A-18 aircraft in the wind tunnel. The active rudder was successful in reducing the buffet responses at the first bending mode around 15 Hz. However, the actuation bandwidth of the rudder is limited. For example, the rudder bandwidth of the F/A-18 aircraft is less than 20 Hz. Therefore, it is not effective for reducing the buffet responses at the second mode around 45 Hz (first torsion mode).

The other technique for active structural control is based on distributed PZT actuators. The piezoelectricity is a property of materials that generate an electrical charge when the materials are subject to material strain, and conversely, PZT materials deform when they are subject to an electrical field. A piezoceramic is therefore capable of acting as either a sensor or actuator. Piezoceramics can be used for control of vibrations by stacking them where excessive vibrations occur. The strain of the structure is fed into a controller that injects voltage into the PZT patches. The mechanical response of the PZT patches due to the input voltage introduces vibrations into the structure, which is set equivalent and opposite to the initially detected one such that the net vibration becomes minimum.

As part of the Actively Controlled Response of Buffet-Affected Tails (ACROBAT) program, Moses [13,14] conducted wind tunnel experiments on 1/6-scale model of the F/A-18 aircraft. The starboard vertical tail was equipped with active rudder, and the port tail was equipped with PZT actuators. The power spectral density (PSD) of the root bending moment at the frequency of the first bending mode was reduced by up to 60%. Recently, Moses et al. [15] tested new sets of actuators, active fiber composite (AFC) actuators and macro-fiber composite (MFC) actuators, for buffet alleviation of 1/6-scale model of F/A-18 aircraft. A total of ten actuators, five per side, were embedded beneath the fiberglass shell of the vertical tail, as shown in Fig. 1. The

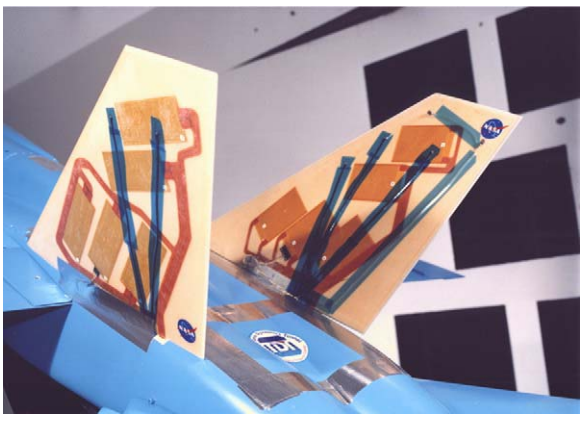

Fig. 1. Photograph of the vertical tails of 1/6-scale model of the F/A-18 aircraft equipped with PZT actuators [15].

new actuators were poled electrically in the plane of the actuators rather than through the thickness. The new actuators performed superbly in reducing structural responses caused by buffet. Additional experiments are currently underway to test the effectiveness of the new actuators in reducing structural responses of full-scale aircraft.

In this study, an active smart material control system for buffet alleviation using distributed PZT actuators is developed. A high-fidelity multidisciplinary computational investigation of active control of the vertical tail buffeting of full-scale model of the F/A-18 aircraft over wide range of angles of attack is conducted and presented. The representative results of several aeroservoelastic models and control laws are discussed in this article.

2. The technical approach

Active control of tail buffeting is a complex multidisciplinary aeroservoelastic problem that involves interaction between several physical and numerical disciplines. The physical disciplines include the fluid dynamics of the vortical flow field over the aircraft, structural dynamics of the flexible structures, electrodynamics of the PZT actuators, and the control law that drive the PZT actuators. The numerical disciplines include grid deformation and fluid–structure interface coupling. In this investigation, the computational modules of these disciplines are integrated into the multidisciplinary computing environment (MDICE) [16]. MDICE controls the temporal synchronization of the data transfer between multidisciplinary analysis modules. The particular sets of analysis modules used in the current investigation are outlined in the following sections.

2.1. The fluid dynamics module

The buffet problem of vertical tails occurs at high angles of attack where the flow field is characterized by strong vortical flow and massive three-dimensional flow separation. Therefore, the problem mandates the solution of the full Navier–Stokes equations to account for vorticity evolution, convection, shedding, and vortex breakdown. The full Navier–Stokes equations are solved using CFD-FASTRAN [17] module using an implicit finite-volume upwind scheme with Roe's flux-difference splitting for spatial differencing and a fully implicit upwind scheme for temporal differencing. On the aircraft surfaces, no-slip and no-penetration conditions are enforced. Riemann's inflow/outflow boundary conditions are assumed at the far field boundaries in all directions. The flow field around the aircraft is assumed symmetric, and therefore, a plane of symmetric boundary condition is used at the symmetry plane.

2.2. The structure dynamics module

The structural dynamic equations of the flexible vertical tail under the influence of the aerodynamics loads of the vortex breakdown flowfield are given by

$$[M_{uu}]\{\ddot{u}\} + [C_{uu}]\{\dot{u}\} + [K_{uu}]\{u\} = \{F\}, \tag{1}$$

where $\{u\}$ is the displacement vector, $[M_{uu}]$ is the mass matrix, $[C_{uu}]$ is the damping matrix, $[K_{uu}]$ is the stiffness matrix, and $\{F\}$ is the aerodynamics force vector. No structural damping is assumed in this investigation. Aerodynamic damping is inherited in the structural-dynamics model since full Navier–Stokes solver is used to compute the aerodynamic force vector.

The structural dynamic equations of the vertical tail, Eq. (1), are solved using three-dimensional finite-element analysis. The vertical tail is modeled using second-order hexahedral elements. The vertical tail is assumed to be the only flexible structure in the aircraft. The initial conditions are the undeformed vertical tail. The vertical tail is assumed clamped at the root and the rudder fin is assumed fixed. The material of the vertical tail is assumed to be aluminum and isotropic. The Young's modulus of elasticity is $4.0 \times 10^{10}\,\mathrm{N/m^2}$, the density is $2765\,\mathrm{kg/m^3}$, and the Poisson's ratio is 0.33. The first structural mode of the vertical tail is first bending mode at 15.5 Hz. The second mode is first torsion mode at 46 Hz, and the third mode is the second bending mode at 54 Hz.

2.3. Finite-element modeling of PZT actuators

The linear PZT constitutive equations, which combine the constitutive equations of solids and dielectric materials into one set of coupled equations, are given by Jaffe et al. [18]

$$\{S\} = [s_E]\{T\} + [d]^{\mathrm{T}}\{E\}, \tag{2}$$

$$\{D\} = [d]\{T\} + [\varepsilon_T]\{E\}, \tag{3}$$

where $[s_E]$ is the compliance matrix, $[d]$ is PZT coupling matrix, $[\varepsilon_T]$ is the dielectric constant matrix (permittivity components), $\{S\}$ is the strain vector, $\{T\}$ is the stress vector, $\{D\}$ is the charge density vector, and $\{E\}$ is the electric field vector. Eq. (2) is the sensor equation, which relates the charge developed in the PZT material to stresses or strains. Eq. (3) is the actuator equation, which relates the applied electric field to the strain developed in the material.

The electric field components, E_k, are related to the electrostatic potential ϕ by the relations:

$$E_k = -\nabla_k \varphi, \quad k = 1, 2, 3. \tag{4}$$

When the variational principle is applied to both the PZT equations and the equations of the solid structure, the linear dynamic equations of the coupled system reduce to the following system of equations:

$$\begin{bmatrix} M_{uu} & 0 \\ 0 & 0 \end{bmatrix} \begin{Bmatrix} \ddot{u} \\ \ddot{\varphi} \end{Bmatrix} + \begin{bmatrix} K_{uu} & K_{u\varphi} \\ K_{\varphi u} & -K_{\varphi\varphi} \end{bmatrix} \begin{Bmatrix} u \\ \varphi \end{Bmatrix} = \begin{Bmatrix} F \\ G \end{Bmatrix}, \tag{5}$$

where u, ϕ, F, and G are the global nodal displacement, electric potential, force, and applied charge vectors, respectively. M_{uu} and K_{uu} represent the mass matrix and stiffness matrix of the original structure, respectively. $K_{u\phi}$ represents the coupled stiffness between electrical field and elastic strain, and $K_{\phi\phi}$ represents the stiffness matrix of the PZT material. These stiffness matrices are given as follows:

$$[K_{u\varphi}] = \int_V B_u^{\mathrm{T}} e B_\varphi \, \mathrm{d}V, \tag{6}$$

$$[K_{\varphi\varphi}] = \int_V B_\varphi^{\mathrm{T}} \varepsilon B_\varphi \, \mathrm{d}V, \tag{7}$$

where ε is the dielectric matrix, and

$$B_u = \begin{bmatrix} \partial/\partial x & 0 & 0 \\ 0 & \partial/\partial y & 0 \\ 0 & 0 & \partial/\partial z \\ \partial/\partial y & \partial/\partial x & 0 \\ 0 & \partial/\partial z & \partial/\partial y \\ \partial/\partial z & 0 & \partial/\partial x \end{bmatrix} [N_u]^{\mathrm{T}}, \tag{8}$$

$$B_\varphi = \begin{Bmatrix} \partial/\partial x \\ \partial/\partial y \\ \partial/\partial z \end{Bmatrix} [N_\varphi]^{\mathrm{T}}, \tag{9}$$

$$[e] = [d][s_E]^{-1}, \tag{10}$$

where N_u and N_ϕ are the shape function matrices for the displacement and electric fields, respectively.

The next step is to define augmented entities for the global displacement field, mass matrix, stiffness matrix, and applied forces. The augmented entities are defined as follows:

$$\tilde{u} = \begin{Bmatrix} u \\ \varphi \end{Bmatrix}, \quad \tilde{M} = \begin{bmatrix} M_{uu} & 0 \\ 0 & 0 \end{bmatrix}, \quad \tilde{K} = \begin{bmatrix} K_{uu} & K_{u\varphi} \\ K_{\varphi u} & -K_{\varphi\varphi} \end{bmatrix}, \quad \tilde{F} = \begin{Bmatrix} F \\ G \end{Bmatrix}. \tag{11}$$

Thus, Eq. (5) may be written as

$$\tilde{M}\ddot{\tilde{u}} + \tilde{K}\tilde{u} = \tilde{F}. \tag{12}$$

Eq. (12) is similar to the original structural dynamic equations of the tail structure, Eq. (1). Therefore, the modifications of the solid finite-element module become as follows: (1) introduce additional nodal dependent variable representing the nodal electrostatic potential, ϕ, and (2) modify the mass and stiffness matrices according to Eq. (11).

2.4. The fluid–structure interfacing module

The fluid–structure interfacing algorithm is used to project the forces from the fluid flow to equivalent forces and moments on the flexible-body structure and to feed back the aeroelastic deflections from the structure nodes to the cells of the flow-field grid. A conservative and consistent interfacing algorithm is used in this investigation [17]. Conservative interfacing enforces the conservation of forces and moments in the interpolation process between two grids. Consistency, or virtual work conservation, requires that the virtual work performed by the solid interface is equivalent to the virtual work performed by the fluid interface. The interfacing is formulated in the most general sense for maximum flexibility. There are no inherent assumptions that the fluid grid is matched with the structure grid, either through different mesh densities or mesh architecture.

2.5. The grid deformation module

The computational grid is deformed every fluid–structure data transfer to accommodate the deformed shape of the tail. The six outer boundary surfaces of the deformed grid block are kept fixed. The grid is deformed using a TransFinite Interpolation algorithm (TFI) [19]. TFI is an interpolation procedure that deforms grids conforming to specified boundaries and it is very computationally efficient. The spacing between grid points is controlled by blending functions that specify how far into the original grid the effect of the new position of the flexible body surfaces is carried. The TFI routine is invoked automatically when a fluid–structure interface is exchanged between application modules.

2.6. The multidisciplinary computing environment

The multidisciplinary modules used in the current investigation are integrated into the MDICE [16]. MDICE is an object-oriented environment that enables the analysis modules to run concurrently and cooperatively on a distributed network of computers. MDICE is used to control the temporal synchronization between the multidisciplinary analysis modules on a distributed environment. Using MDICE environment, one can avoid giant monolithic codes that attempt to provide all modules in a single large computer program. Such large programs are difficult to develop and maintain and by their nature cannot contain up-to-date technology.

3. Computational aeroservoelastic model

The computational aeroservoelastic model of the F/A-18 aircraft consists of three main parts. The first part is geometry modeling of a full-scale model of the F/A-18 aircraft. The second part is a PZT aeroservoelastic model of the vertical tail. The third part is a control law to drive the PZT actuators.

3.1. F/A-18 geometry modeling

The geometry of a full-scale model of the F/A-18 aircraft is modeled using a structured body-fitted grid system with one-to-one grid connectivity. The surface grid of the F/A-18 aircraft is shown in Fig. 2. The grid is a multiblock H-H grid consisting of 53 structured blocks utilizing 2.56 million cells (2.68 million grid points). The global grid extends 5 wing chords upstream and downstream of the aircraft, and 8 wing chords normal to the aircraft. The grid is clustered near the apex and leading edge of the wing LEX in order to produce robust and well-defined leading-edge vortices.

For the structural dynamics analysis, the vertical tail of the F/A-18 aircraft is modeled using second-order brick (hexahedral) elements. In general, the surface grid of the vertical tail for the computational structural dynamics computations and computational fluid dynamics computations are not identical. The forces and deflections are interpolated between the two grids using the interfacing module discussed before.

3.2. Aeroservoelastic model of the vertical tail

The inboard and outboard surfaces of the aeroservoelastic model of the F/A-18 vertical tail are shown in Fig. 3. A total of five PZT actuators are shown on every side of the vertical tail. The root PZT actuators (3 per side) were strategically located near the tail root to alleviate the buffeting in the first bending mode. The tip PZT actuators (2 per side) were located near the tail tip and aligned directionally to alleviate the buffeting in the first torsion mode. The two stacks of actuators on both sides of the tail are set in an opposite phase to each other to generate bending and torsion. In other words, when one side of the tail is contracting the other side of the tail is expanding to generate either bending or torsion. Each set of PZT actuators on both sides of the tail is being commanded by a control law to strain in opposite directions simultaneously to enable the vertical tail to bend. The acceleration at a near-tip point (75% span and 80% chord) is recorded and used as the input signal to the control law.

The ceramic PZT patches used in this computational study are assumed to be the MFCs [20]. The PZT fibers (PZT-5A) of the MFC are transversely aligned in order to sense and actuate in-plane stresses and strains for structural actuation. The material properties of the MFC were obtained from Wilkie et al. [20] and Azzouz et al. [21]. The material properties are given in Table 1.

3.3. The control law

The block diagram of the active control system used for tail buffeting alleviation is shown in Fig. 4. The control law is a single-input/single-output control law that utilizes a feedback signal from an accelerometer

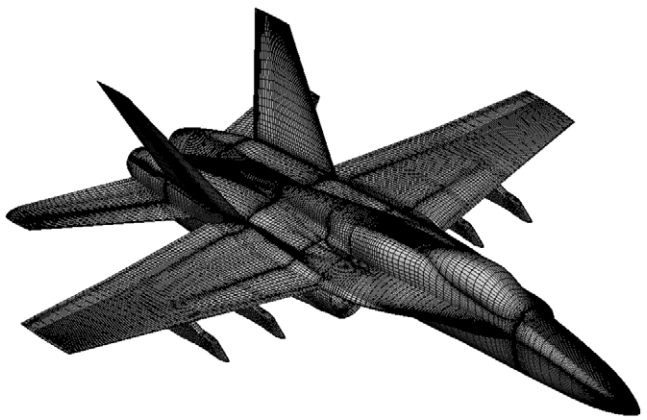

Fig. 2. Surface grid over the F/A-18 aircraft model.

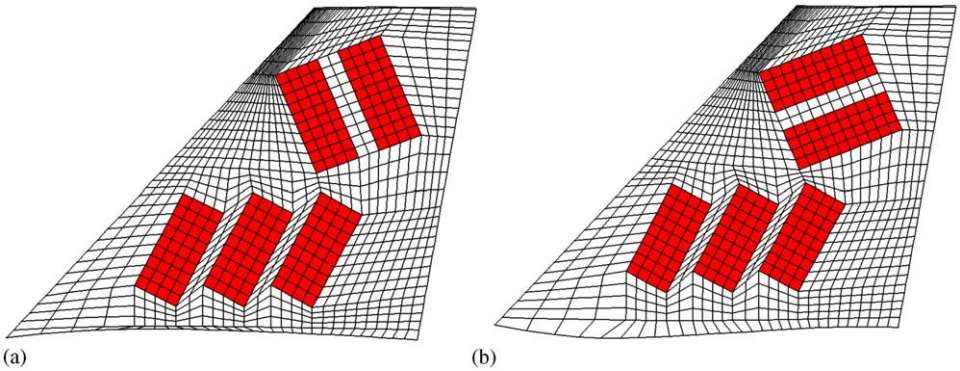

Fig. 3. Aeroservoelastic model of the vertical tail: (a) inboard surface, (b) outboard surface.

Table 1
Material properties of the PZT patches

Properties	MFC	Units
d_{11}/d_{31}	530 E−12	m/V
d_{12}/d_{32}	−210 E−12	m/V
E_1	3.65 E+10	N/m^2
E_2	0.76 E+10	N/m^2
G_{12}	1.46 E+10	N/m^2
G_{23}	0.73 E+10	N/m^2
K_{11}	495	—
v_{12}	0.25	—
ρ	7552	kg/m^3
Thickness	0.13	in

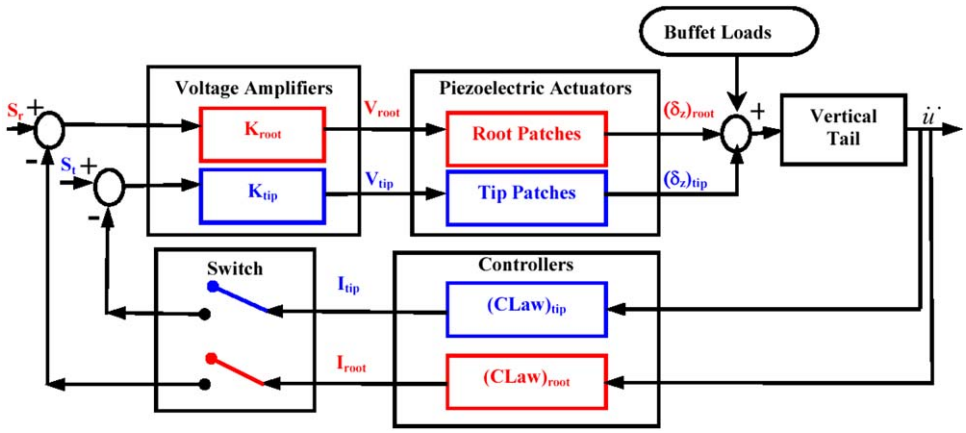

Fig. 4. Active control system diagram used for tail buffet alleviation.

mounted near the tip of the vertical tail. The measured acceleration of the vertical tail, $\ddot{u}$, is fed through the controller into two control laws, $(\mathrm{CLaw})_{\mathrm{tip}}$ and $(\mathrm{CLaw})_{\mathrm{root}}$ of the tip and root PZT patches, respectively. Each of the control laws has different control law gain, which is used to set the peak magnitude of the control law to unity. A switch is used to close or open the control loop of either the tip or the root control law. The outputs

of the controllers, I_{tip} and I_{root}, are sent to a summing junction where they may be combined with other signals for system identification. The signal is then sent into voltage amplifiers with gains of K_{tip} and K_{root}. The voltage amplifiers are used to increase the magnitude of the voltage signal to a value within the operational range of the actuators. The voltage signal is then applied to drive the PZT actuators causing strain actuation. The input to the vertical tail is therefore the strain actuation of the PZT patches in addition to the aerodynamics buffet loads.

The aerodynamic buffet loads are being input to the vertical tails through the unsteady surface pressure signals on both sides of the vertical tail. The root mean square (RMS) of the differential pressure and the predominant non-dimensional frequency of buffet pressure peaks on the surface of the vertical tail at a point located at 45% chord and 60% span are shown in Fig. 5. The results are compared with flight and wind tunnel data reported by Meyn et al. [22]. The results compared well with the experimental and flight test data over the angles of attack range. The figure shows that the peaks of the buffet excitation shift into lower frequencies as the angle of attack increases. The figure also shows that the maximum buffet condition occurs around the 30° angle of attack. The PSD of the differential pressure at the 30 × angle of attack is shown in Fig. 6. As shown in the figure, the peak value of the PSD occurs at 16 Hz, which is very close to the first bending mode of the vertical tail structure. Therefore, the control law used to drive the root PZT actuators is designed to produce maximum magnitude at 16 Hz, near the first bending mode of the structure. If the structural model is modified to include structural damping, no modification to the control law is necessary. That is because structural damping affects only the amplitude of vibrations, not the frequency. In that case, the control law will still provide maximum input magnitude at the predominant frequency. However, the suppression effect is expected to increase due to the additional structural damping.

The frequency responses of the control laws, $CLaw_{root}$ and $CLaw_{tip}$, are shown in Fig. 7. The peak magnitude is intentionally set to unity so that adjustments to the magnitude could be made via the gain block K_{root} and K_{tip}. The phase of the control law near the modal frequency of interest is set to −90° to augment structural damping. Two control laws were designed for the root and tip PZT actuators to control tail buffeting in the first bending and first torsion modes. The control laws for the root and tip PZT actuators are designed to produce maximum input magnitude at the first bending mode (16 Hz) and the first torsion mode (46 Hz), respectively. The single-input/single-output controllers were designed using low pass filtering for the root controller and band pass filtering for the tip controller. The filtering are used so as not to excite the other modes when feedback is turned on as well as to concentrate the amplifier energy near the modal frequencies of interest.

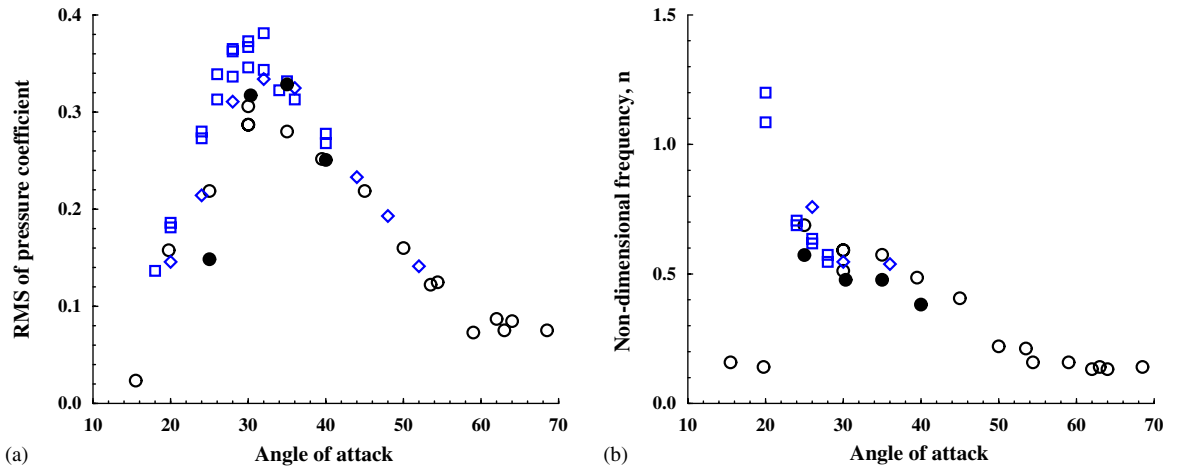

Fig. 5. (a) RMS of differential pressure coefficient signal; and (b) predominant non-dimensional frequency of buffet pressure peaks at 45% chord and 60% span of the vertical tail: ○, flight data [22]; □, full-scale model [22]; ◇, 12% scale model [22]; ●, present computation.

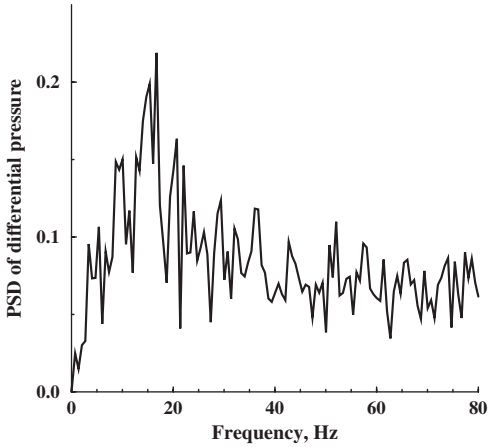

Fig. 6. PSD of differential pressure signal at 45% chord and 60% span of the vertical tail. The aircraft model is set at 30° angle of attack.

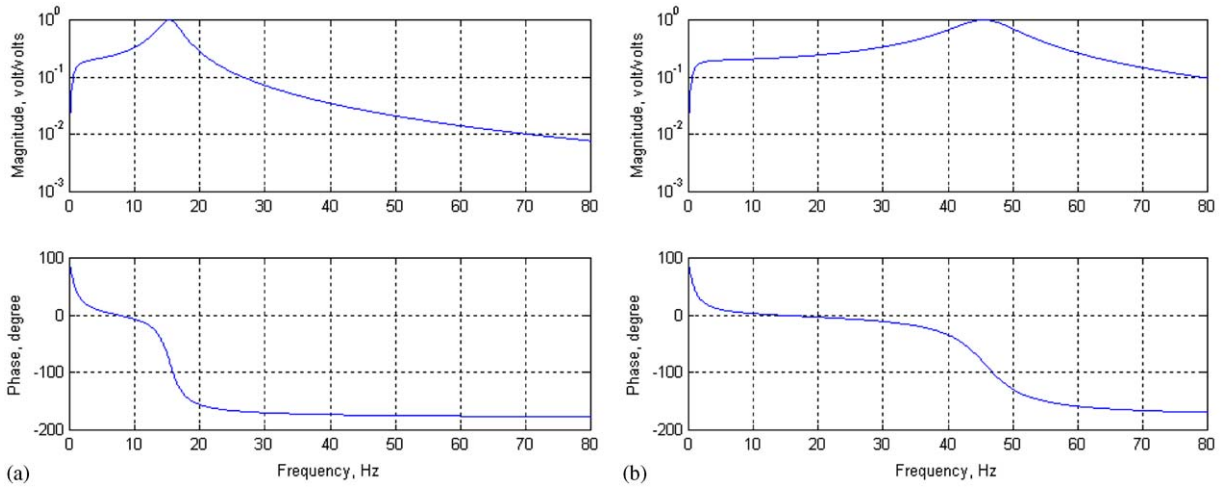

Fig. 7. Frequency response of the controllers: (a) $CLaw_{root}$ for the root PZT actuators, (b) $CLaw_{tip}$ for the tip PZT actuators.

4. Results and discussion

The aeroservoelastic model discussed above is used to study the effect of the distributed PZT actuators on the vertical tail buffeting near the maximum buffet condition. The PSD of the tail-tip accelerations is used to compare open-loop and closed-loop results. At Mach number of 0.243 and Reynolds number of 11 million, the maximum buffet loads for the full-scale F/A-18 aircraft model is found to occur around the 30° angle of attack as presented previously. The flowfield at this angle of attack is characterized by strong vortical flow, massive flow separation, and unsteady vortex breakdown. Three-dimensional and front view snapshots of the vortical flow over the aircraft at 30° angle of attack are shown in Fig. 8. As shown in the figure, the vortex cores of the LEX and wing vortices break down ahead of the vertical tails. The spiral motion of the vortex cores and the abrupt kink in the vortex pathline indicates the vortex breakdown. The figure shows clearly that the vortex breakdown flow impinges upon the surfaces of the vertical tail; a typical buffet condition.

This multidisciplinary aeroelastic problem is solved using two consecutive steps: the first step solves for the vortical flow field characteristics around the rigid aircraft configuration. The initial condition of this step is the undistributed free-stream condition everywhere. The solution is carried out until the changes in the vortical

flow field become insignificant. The second step solves for the unsteady aerodynamic flowfield and aeroelastic responses of the flexible configuration. The initial condition of this step is the final solution of the first step. In the second step, strong coupling between the fluid and structure is considered. The time steps of the computations are fixed in all cases at 10^{-4} s. The problem is solved on a Linux computer cluster of six units. The total grid is divided almost evenly between the six processors using domain decomposition. The speed of each processor is 1.0 GHz. Every partition of the grid requires approximately 160 MB of memory. The computational cost is about 40 μs per time step per grid point.

4.1. *Buffeting alleviation results*

In this part of the investigation, the aeroservoelastic model shown in Fig. 3 is used along with the control law shown in Fig. 7 to control the buffet problem at 30° angle of attack. The PSD of the acceleration signal is computed based on a time span of two seconds of simulation corresponding to 20,000 sample points and resolution frequency of about 0.6 Hz. The length of the time record is fairly sufficient since there are no abrupt changes in the signal and the vertical tail response is nearly periodic [17].

The effects of closed-loop control (feedback on) on the PSD of tail-tip accelerations are shown in Fig. 9. In this case, the feedback is applied only to the root PZT actuators, and no signal is applied to the tip PZT actuators. As shown in the figure, the peak magnitude of the closed-loop (feedback on) buffeting is lower than

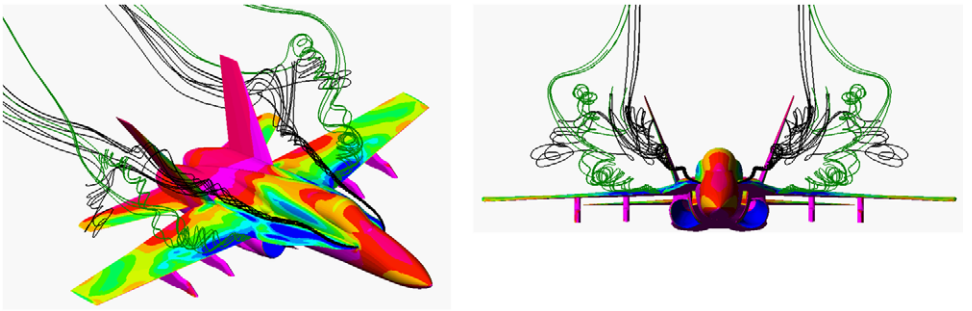

Fig. 8. Three-dimensional and front view snapshots of the interaction between the instantaneous streamlines of the vortical flow and the vertical tails of the aircraft model.

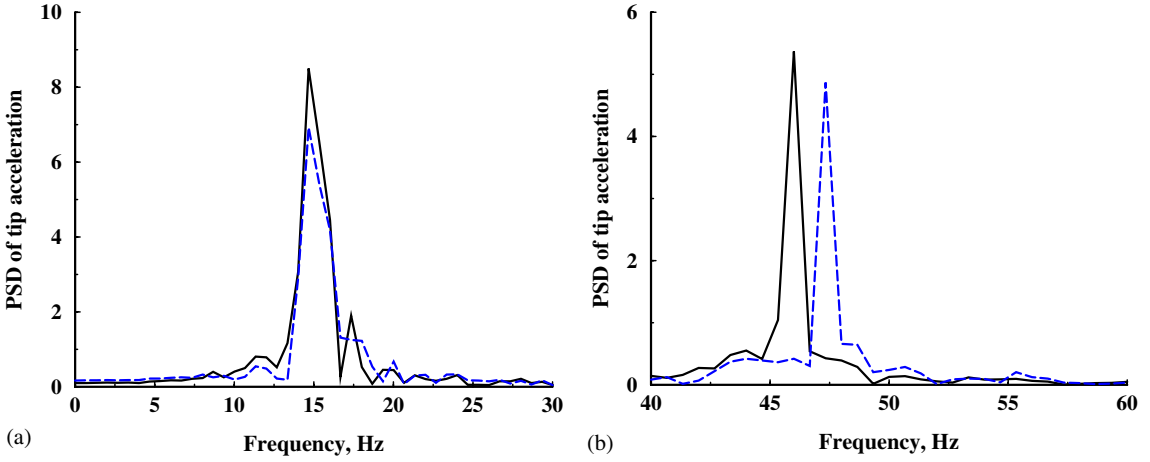

Fig. 9. PSD of tail-tip acceleration using feedback control to the root PZT actuators only: (a) PSD near bending mode frequency; (b) PSD near torsion mode frequency; ——, open loop; - - -, closed loop.

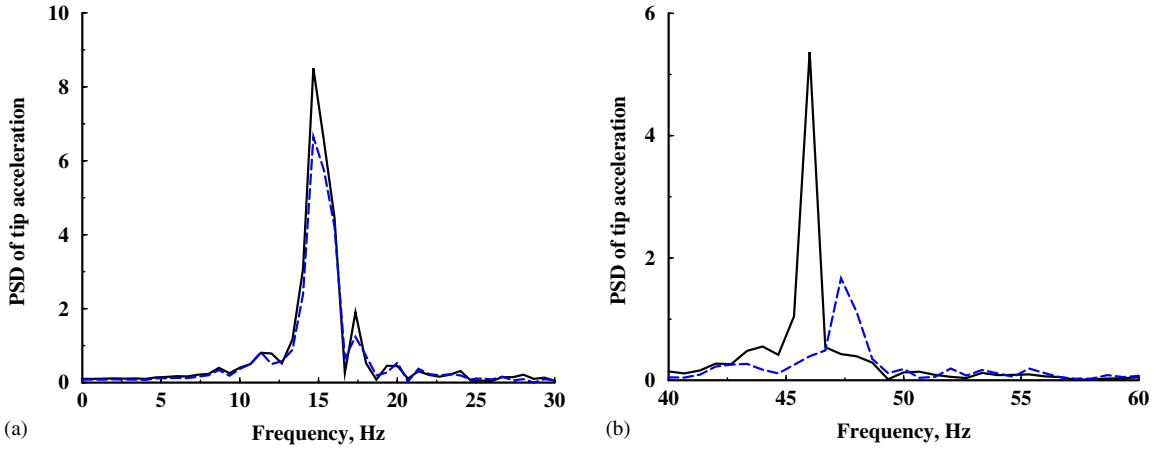

Fig. 10. PSD of tail-tip acceleration using feedback control to the root and tip PZT actuators: (a) PSD near bending mode frequency; (b) PSD near torsion mode frequency: ——, open loop; - - -, closed loop.

the peak magnitude of the open-loop (feedback off) buffeting for frequencies near the first bending and torsion modes. The PSD peak magnitude of the tail-tip acceleration in the first bending mode is reduced by about 18%. The RMS value of tail-tip acceleration is reduced by about 4%. The PSD peak magnitude of the tip acceleration in the first torsion mode is also reduced by about 9.5%, although no input command is applied to the tip PZT actuators. This reduction is caused by excitation at the first torsion mode caused by the feedback controller at the first bending mode. The increase in magnitude around 47.5 Hz is caused by the control law and could have been prevented by modifying the control law to adjust the phase in that region of the spectra.

Next, closed-loop controls are applied to both the root and tip PZT actuators. In this case, the PSD of the tail-tip acceleration is shown in Fig. 10. The peak magnitude of the closed-loop buffeting in the first torsion mode is considerably lower than the peak magnitude of the open-loop buffeting. The PSD peak magnitude of the tail-tip acceleration in the first torsion mode is reduced by about 69%. The RMS value of tail-tip acceleration is reduced by about 10%. The PSD peak magnitude of the tail-tip acceleration in the first bending mode is also reduced by about 22%. Similar to the previous case, there is a frequency shift at the first torsion mode caused by the phase of the control law. These figures clearly show that the PZT actuators are much more effective in reducing the peak magnitudes at the first torsion mode than those at the first bending mode. This is in agreement with the experimental observations of Moses [13,14].

The reason that the PZT actuators are less effective for the first bending mode can be explained from the distribution of the strain energy and the stiffness of the tail structure. In the first bending mode, the strain energy of the vertical tail is concentrated near the root of the tail. The PZT actuators are not as effective near the tail root because of the large structural stiffness near the root. In the first torsion mode, the strain energy is concentrated near the upper third of the tail where the structural stiffness is significantly lower than the stiffness at the tail root.

The time history of the tip deflection at the 75% span and 80% chord point of the vertical tail, for the first one-half seconds of simulation, are shown in Fig. 11 for both the open-loop and closed-loop cases. The closed-loop controller is shown to reduce the amplitude of the tip deflection. The figure also shows that it takes almost half a second before the effect of the closed-loop controller shows up. The time history of the tip acceleration (input signal to the control laws) and the time history of the input command signal to the root and tip PZT actuators (output signal of the control laws) in volts are shown in Fig. 12. A maximum of almost 2000 V are kept for both signals, which is well within the operational range of the PZT actuators.

4.2. *Effect of integrator control law*

In this section, the effect of a simple integrator control law on the tail-tip acceleration is investigated. In the integrator control law, the transfer function of the control law is simply set to $G(s) = 1/s$. The reason the

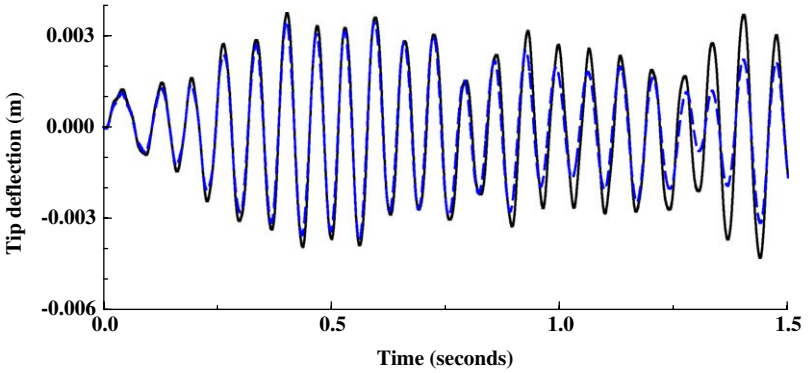

Fig. 11. The time history of the vertical tail-tip deflection using feedback control to the root and tip PZT actuators: ——, open loop; - - -, closed loop.

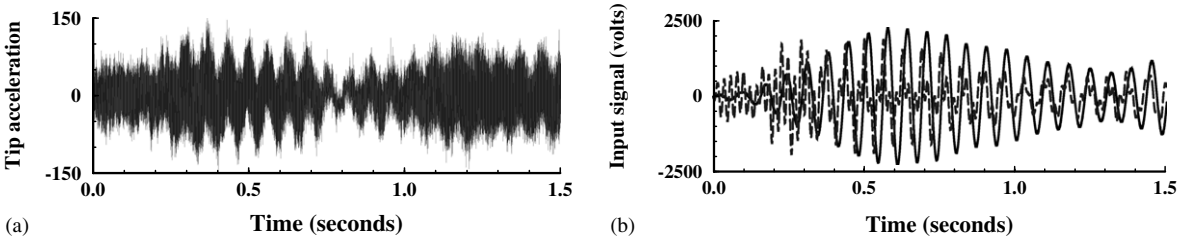

Fig. 12. The time history of (a) tail-tip acceleration and (b) the input signal to the PZT actuators: ——, root PZT; - - -, tip PZT.

integrator control law is tested here is that a pure integrator will give an upper bound to the active damping, especially when an accelerometer signal is fed back to the controller. The magnitude of an integrator drops off linearly with frequency, while providing constant -90° phase lag for all frequencies. However, depending on the frequencies of the other modes, there may be sufficient gain to react considerably to those other frequencies. In practice, integrator control law would only be used when the location of the accelerometer naturally isolates the mode of interest from the total multimode acceleration signal. The reason is that the integrator can become saturated quickly if it tries to respond to all modes, especially those at high frequencies.

The PSD of the tail-tip acceleration is shown in Fig. 13 when closed-loop integrator controllers are applied to both the root and tip PZT actuators. The PSD peak magnitude of the tail-tip acceleration in the first bending mode is reduced by about 7%. The RMS value of tip acceleration is reduced by about 12%. The PSD peak magnitude of the tip acceleration in the first torsion mode is also reduced by about 38%.

4.3. Alternative setup of the aeroservoelastic model

The PZT setup in the aeroservoelastic model shown in Fig. 3 is similar to the one used for the 1/6-scale model of the F/A-18 aircraft by Moses et al. [15]. However, for the full-scale model, the size of the patches may be too large to be manufactured. Therefore, an alternative setup of the PZT actuators in the aeroservoelastic model of the F/A-18 vertical tail was assumed using smaller-size PZT patches of approximately 7 in long and 3 in wide. In this model, shown in Fig. 14, 96 PZT patches (48 per side) were distributed over the inboard and outboard surfaces of the vertical tail. The root PZT actuators (36 per side) and the tip PZT actuators (12 per side) were directed in the same way as the other aeroservoelastic model as to damp structural vibrations in the first bending and torsion modes, respectively. The PZT patches are poled electrically along the plane of the actuators, similar to the previous model. The control laws that are used to drive these PZT actuators are similar to those used with the previous model.

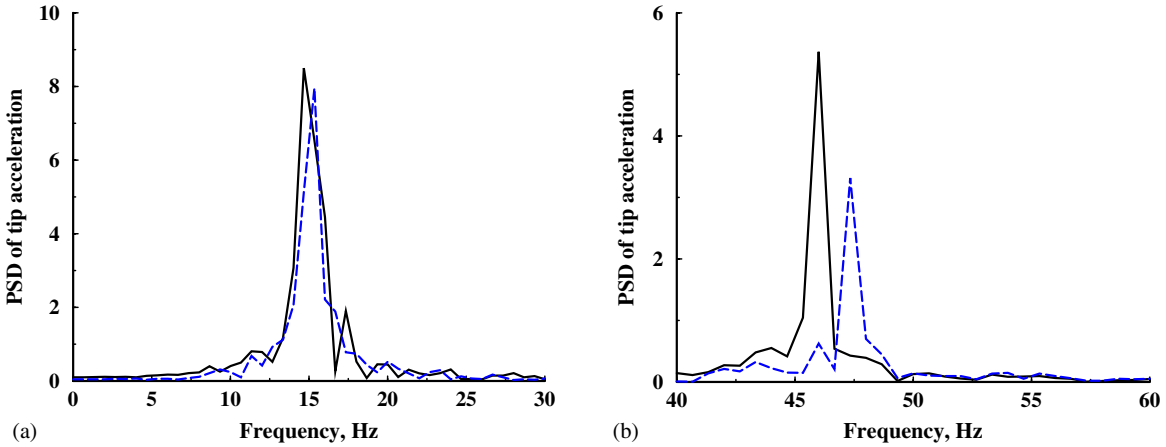

Fig. 13. PSD of tail-tip acceleration using integrator feedback control to the root and tip PZT actuators: (a) PSD near bending mode frequency; (b) PSD near torsion mode frequency: ——, open loop; - - -, closed loop.

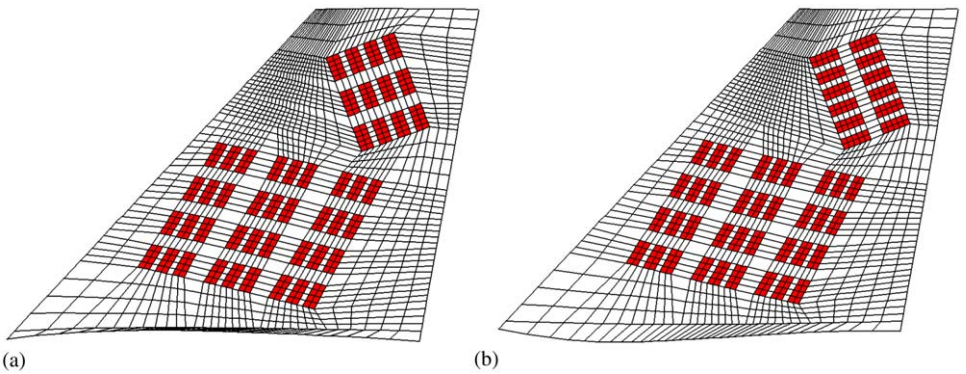

Fig. 14. An alternative PZT setup on the aeroservoelastic model of the F/A-18 vertical tail: (a) inboard surface, (b) outboard surface.

The PSD of the tail-tip acceleration is shown in Fig. 15 when feedback signals are applied to both the root and tip PZT actuators. Maximum input voltage commands of 2000 V are applied to both the root and tip PZT actuators, similar to the other aeroservoelastic model. The PSD peak magnitude of the tail-tip acceleration in the first torsion mode is reduced by about 82%. The RMS value of tip acceleration is reduced by about 12%. The PSD peak magnitude of the tip acceleration in the first bending mode is also reduced by about 7%. This shows that this PZT setup of the aeroservoelastic model is more effective than the other model in reducing the peak magnitude of acceleration in the first torsion mode. However, it is less effective in the first bending mode. One reason for the poor performance at the first bending mode is that the PZT patches near the root of the vertical tail are located in higher locations than those of the previous setup shown in Fig. 3.

4.4. Effect of PZT actuators over angles of attack

The effect of the PZT actuators for buffeting control over wide range of angles of attack is shown in Fig. 16. The figure shows the peak values of the PSD of the tail-tip acceleration at the first bending and torsion modes of the vertical tail. A constant gain setting is used for each actuator at all angles of attack. The PSD peak values reported in Fig. 16 are normalized by the maximum peak value computed within the angles of attack range considered in this investigation. The figure clearly shows that the actively controlled PZT actuators provided considerable damping to the vertical tail along the angles of attack range. The PSD peak of the tail-tip acceleration is reduced by as much 22% at the first bending mode and is reduced by as much as 90% at the

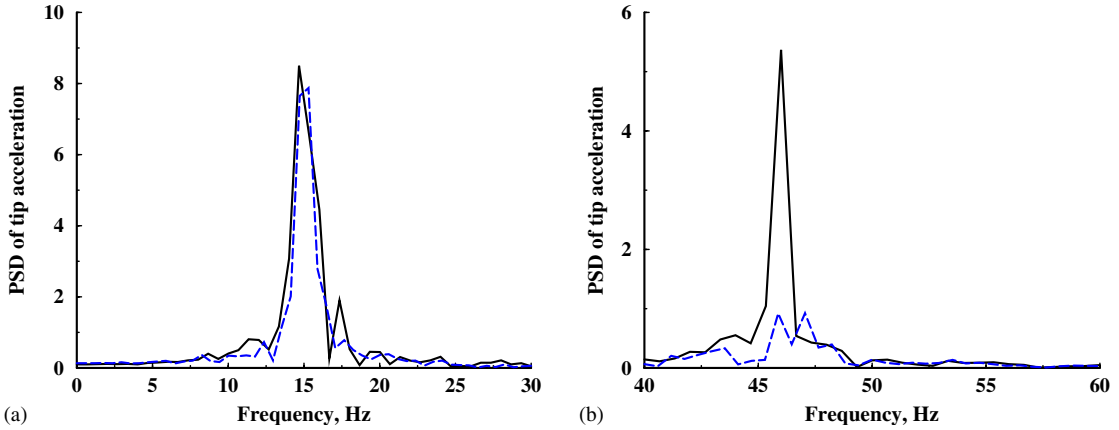

Fig. 15. PSD of tail-tip acceleration using feedback control to the root and tip PZT actuators on the alternative aeroservoelastic model: (a) PSD near bending mode frequency; (b) PSD near torsion mode frequency; ——, open loop; - - -, closed loop.

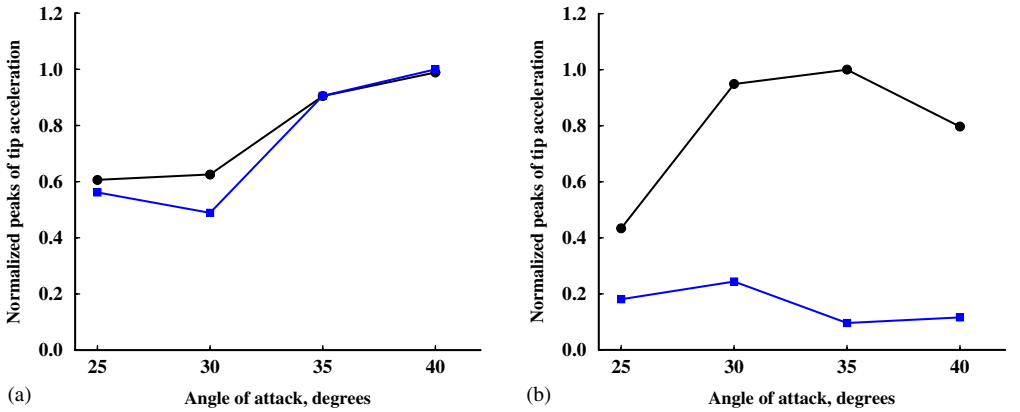

Fig. 16. Normalized peaks of the PSD of the tail-tip acceleration over several angles of attack: (a) PSD peaks at first bending mode; (b) PSD peaks at first torsion mode; —●—, open loop; —■—, closed loop.

first torsion mode. The figure clearly shows that the actively controlled PZT actuators are very effective at the first torsion mode over wide range of angles of attack. The effectiveness of the actively controlled PZT actuators to add damping at the first bending mode appears to be diminishing as angle of attack is increased above 30° angle of attack. Moses [14] observed similar trend in the wind tunnel using the 1/6-scale model of the F/A-18 aircraft.

5. Conclusion

An active smart material control system environment has been developed to control vertical tail buffeting of fighter aircraft at wide range of angles of attack. A computational investigation has been conducted to control tail-buffeting responses of full-scale F/A-18 aircraft using distributed piezoelectric (PZT) actuators. The PZT actuators were strategically located over the inboard and outboard surfaces of the vertical tail to alleviate the tail buffeting in the first bending and torsion modes. The results of this investigation indicated that the PZT actuators are more effective in reducing the structural responses in the first torsion mode than those in the first bending mode. At 30° angle of attack, RMS values of the tail-tip acceleration were reduced by as much as 12%. The PZT actuators reduced the power spectral density peaks of the tip acceleration by up to 22% in the

first bending mode and by up to 82% in the first torsion mode. The actively controlled PZT actuators were also effective over wide range of angles of attack.

References

[1] B. Lee, D. Brown, M. Zgela, D. Poirel, Wind tunnel investigation of tail buffet on the F-18 aircraft, *AGARD-CP*-483, 1990.
[2] L.A. Meyn, K.D. James, Full scale wind tunnel studies of F/A-18 tail buffet, *AIAA Paper* 93-3519, 1993.
[3] C. Pettit, D. Brown, E. Pendleton, Wind tunnel tests of full-scale F/A-18 twin tail buffet: a summary of pressure and response measurements, *AIAA Paper* 94-3476, 1994.
[4] R.W. Moses, L.J. Huttsell, Fin buffeting features of an early F-22 model, *AIAA Paper* 2000-1695, 2000.
[5] E.F. Sheta, L.J. Huttsell, Numerical analysis of F/A-18 vertical tail buffeting, *AIAA Paper* 2001-1664, 2001.
[6] G.H. Shah, Wind-tunnel investigation of aerodynamic and tail buffet characteristics of leading-edge extension modifications to the F/A-18, *AIAA Paper* 91-2889, 1991.
[7] B. Lee, N. Valerio, Vortical flow structure near the F/A-18 LEX at high incidence, *Journal of Aircraft* (1994) 1221–1223.
[8] D. Rao, C. Puram, G. Shah, Vortex control for tail buffet alleviation on a twin-tail fighter configuration, *SAE Paper* 892221, 1989.
[9] E.F. Sheta, Buffet alleviation of F/A-18 aircraft using LEX fences, *AIAA Paper* 2003-1888, 2003.
[10] E.F. Sheta, L.J. Huttsell, Control of F/A-18 vertical tail buffeting by vortical blowing, *AIAA Paper* 2002-0948, 2002.
[11] E.F. Sheta, V.J. Harrand, L.J. Huttsell, Active vortical flow control for alleviation of twin-tail buffet of generic fighter aircraft, *Journal of Fluids and Structures* (2001) 769–789.
[12] H. Ashley, H. Rock, R. Digumarthi, K. Chaney, A. Eggers, Active control for fin buffet alleviation, *WL-TR*-93-3099, 1994.
[13] R.W. Moses, Active vertical tail buffeting alleviation on an F/A-18 model in a wind tunnel, *Second Joint NASA/FAA/DOD Conference on Aging Aircraft*, Williamsburg, VA, 1998.
[14] R.W. Moses, Vertical tail buffeting alleviation using piezoelectric actuators—some results of the actively controlled response of buffet-affected tails (ACROBAT) program, *NASA TM* 110336, 1997.
[15] R.W. Moses, C.D. Wiesman, A.A. Bent, A.E. Pizzochero, Evaluation of new actuators in a buffet loads environment, *CEAS/AIAA/AIAE International Forum on Aeroelasticity and Structural Dynamics*, Madrid, Spain, 2001.
[16] G.M. Kingsley, J.M. Siegel, V.J. Harrand, C. Lawrence, J. Luker, Development of the multi-disciplinary computing environment (MDICE), *AIAA Paper* 98-4738, 1998.
[17] E.F. Sheta, Prediction and control of twin-tail buffet of fighter aircraft, *AirForce Research Laboratory Technical Report* AFRL-VA-WP-TR-2002-3049, 2002.
[18] B. Jaffe, R. Cook, H. Jaffe, *Piezoelectric Ceramics*, Academic Press, New York, NY, 1971.
[19] J.F. Thompson, B.K. Soni, N.P. Weatherill, *Handbook of Grid Generation*, CRC Press, Boca Raton, FL, 1998 pp.3.1–3.15.
[20] W.K. Wilkie, R.G. Bryant, J.W. High, R.L. Fox, R.F. Hellbaum, A. Jalink, B. Little, P. Mirick. Low-cost piezocomposite actuator for structural control applications, *SPIE Seventh International Symposium on Smart Structures and Materials*, 2000.
[21] M.S. Azzouz, J.S. Bevan, J.J. Ro, C. Mei, Finite element modeling of MFC/AFC actuators, *SPIE Eighth International Symposium on Smart Structures and Materials*, 2001.
[22] L.A. Meyn, K.D. James, R.J. Green, Correlation of F/A-18 tail buffet results, *High Alpha Projects and Technology Conference, Dryden Flight Research Center*, 1994.